Science Advances
AAAS

advances.sciencemag.org/cgi/content/full/5/12/eaax3777/DC1

Supplementary Materials for

High-contrast and reversible polymer thermal regulator by structural phase transition

Ramesh Shrestha, Yuxuan Luan, Sunmi Shin, Teng Zhang, Xiao Luo, James S. Lundh, Wei Gong, Michael R. Bockstaller, Sukwon Choi, Tengfei Luo, Renkun Chen, Kedar Hippalgaonkar, Sheng Shen*

*Corresponding author. Email: sshen1@cmu.edu

Published 13 December 2019, *Sci. Adv.* **5**, eaax3777 (2019)
DOI: 10.1126/sciadv.aax3777

This PDF file includes:

Supplementary Text

1. Thermal switching of existing materials

Table S1 lists the data of the thermal switching ratios plotted in Fig. 2C of the main paper. The first column shows the material used for thermal switches. The second and the third columns show the switching ratio and the corresponding reference, respectively.

Table S1. Data of the switching ratios of the thermal switches in Fig. 2C.

Material	Switching Ratio	Reference
nCB	1.33	(*31*)
VO_2	1.5	(*26*)
Ni–Mn–In alloys	1.5	(*13*)
K	1.8	(*32*)
c-Se	1.8	(*33*)
C_6H_{14}	2	(*34*)
Sn	2	(*15*)
Zn	2	(*32*)
In	2.2	(*15*)
$LiNO_3$	2.3	(*15*)
Cd	2.4	(*32*)
$C/C_{16}H_{34}$ composite	3	(*17*)

$Ge_2Sb_2Te_5$	3.3	(*27*)
Azobenzene polymers	3.5	(*14*)
Hg	4	(*32*)

2. Switching ratios of PE nanofiber samples

Switching ratio is determined by linear fitting at the phase transition region, as shown in fig. S1. The data points nearest to the fitted line around the phase transition starting and ending temperatures are used to determine G_{on} and G_{off}, respectively. Switching ratio is calculated by G_{on}/G_{off}. Uncertainty is determined by error propagation formula. Table S2 presents the switching ratios of 5 samples, in which samples I-IV correspond to nanofibers #1-4 in the manuscript, respectively. The first column is the sample number. The second column is the switching ratio with the corresponding uncertainty.

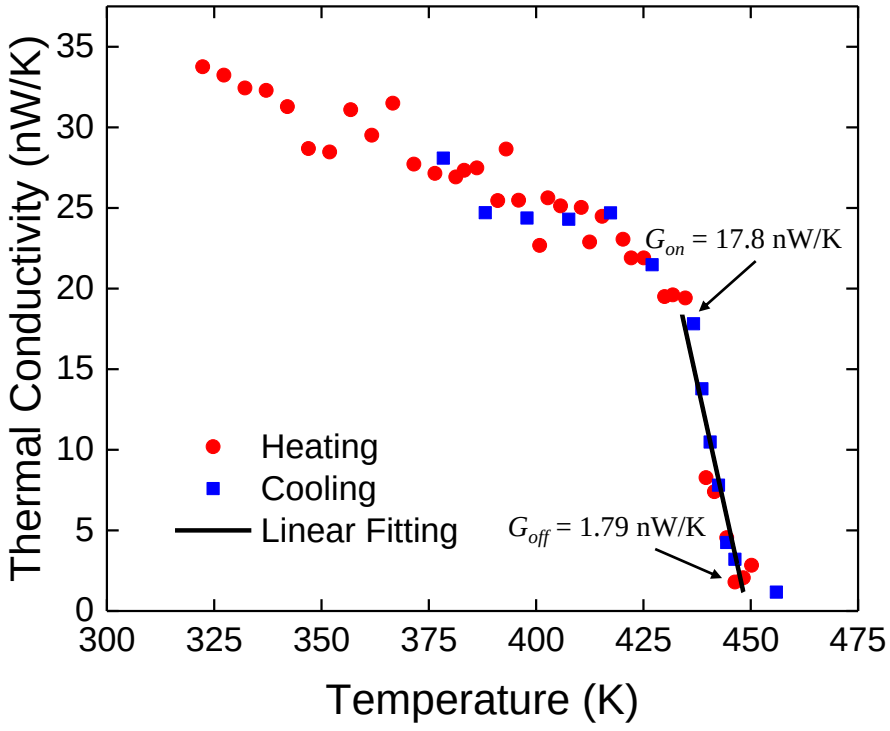

Fig. S1. Determination of G_{on} and G_{off}.

Table S2. Data of the switching ratios of multiple samples.

No.	Switching Ratio	Phase Transition Temperature (K)
I	9.9 ± 1.8	432
II	9.9 ± 0.6	444
III	8.4 ± 3.4	435
IV	6.1 ± 0.9	440
V	5.6 ± 0.7	435

3. Phase transition in a PE microfiber

As seen in fig. S2, the thermal conductance of a PE microfiber drops sharply at ~430 K and shows the switching behavior, which implies that this transition exists in the PE microfiber. However, upon cooling the microfiber from ~450 K to ~410 K, the thermal switching ratio is degraded, indicating that the phase transition of the microfiber is not completely reversible and shows hysteresis. This limits the performance of a PE microfiber thermal switch compared to a PE nanofiber. The irreversibility of the thermal conductance in a PE microfiber is because of the lower degree of crystallinity in a microfiber than that in a nanofiber. This causes the phase transition temperature range of a microfiber to overlap with its melting temperature range. Additionally, the amorphous regions in a microfiber could easily relax the constraints on aligned crystallites which is necessary for the complete reversibility.

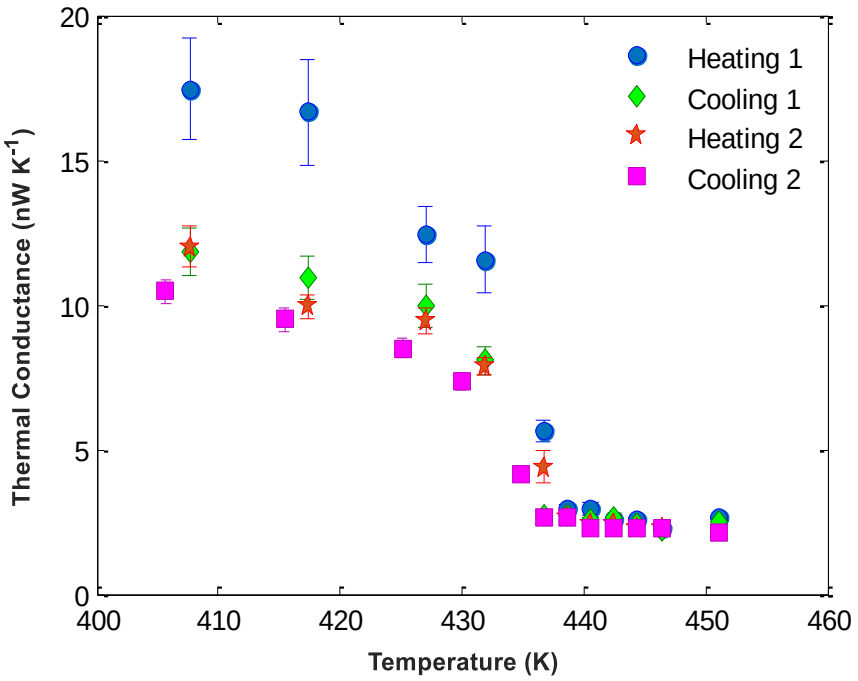

Fig. S2. Thermal conductance measurement of a PE microfiber in two heating/cooling cycles.

4. Phase transition of PE nanofibers at different heating rates

To investigate the effect of heating rates on the phase transition and its corresponding switching ratio, we performed the thermal measurements of a single PE nanofiber at different heating rates in which the dc current rate of the heating island in the micro thermal device varied from 0.01 μA/step to 0.5 μA/step. As shown in fig. S3, the measured heat flow Q is plotted as a function of temperature difference ΔT for four different current rates of 0.01 μA/step, 0.05 μA/step, 0.1 μA/step, and 0.5 μA/step. The time of each step is 20 seconds for all the heating rates (0.01-0.5 μA/step). In fig. S3, the four Q-ΔT curves almost overlap with each other, manifesting that the switching ratios presented in this manuscript are not affected by the selected heating rates in our experiment.

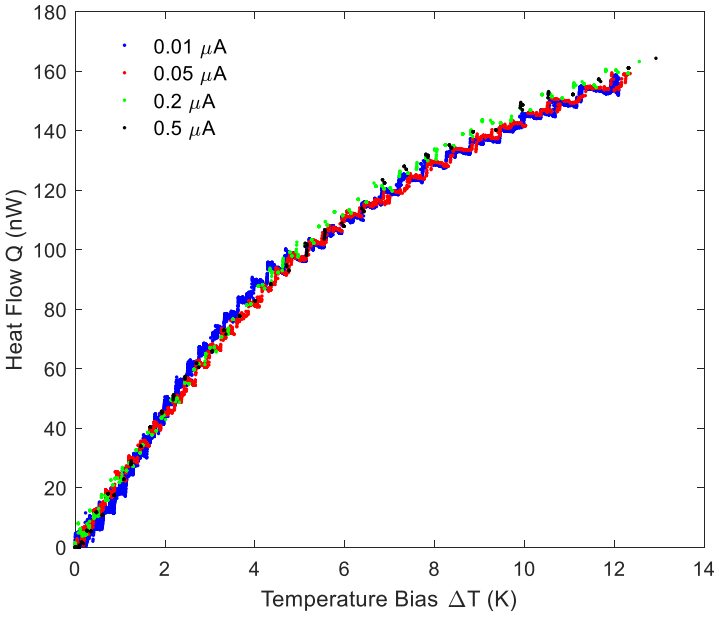

Fig. S3. Heat flow versus temperature bias at different heating rates. The environmental temperature is fixed at 445 K.

5. Thermal stability of PE nanofibers

To find the temperature at which the PE nanofiber starts to show the irreversible structural change, we conduct multiple temperature sweeps in which its thermal conductance is measured up to different maximum temperatures. As seen in fig. S4, the nanofiber sample displays the partially irreversible phase change when the temperature reaches around 525 K because the measured thermal conductance does not trace back to the initial value in the next temperature sweep. The nanofiber shows the completely irreversible structural change when the temperature reaches 555 K. After that, the measured thermal conductance is not temperature-dependent, behaving like an amorphous sample.

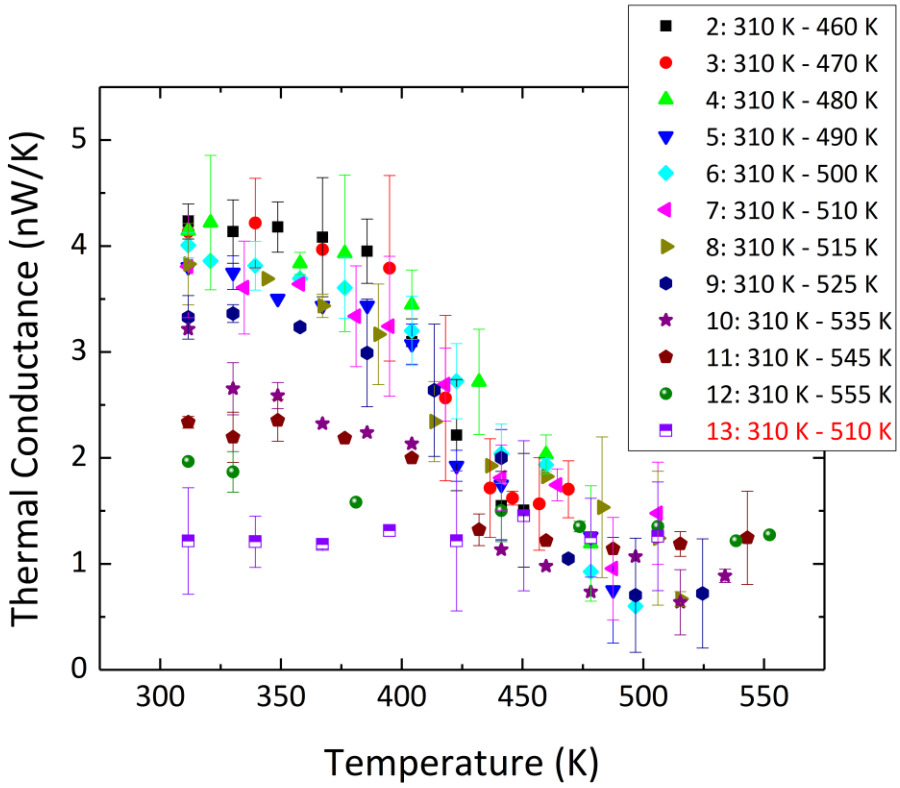

Fig. S4. Multiple temperature sweeps of a PE nanofiber. The 1st thermal measurement is the anneal process. The data sets (2-13) are the temperature sweeps. This fiber starts to show irreversible structural change when the temperature increases to 525 K and fully irreversible structural change when the temperature reaches 555 K.

6. Molecular dynamics (MD) simulations of PE nanofibers

In this work, molecular dynamics (MD) simulations are used to understand the phase transition phenomena in PE nanofibers. The polymer consistent force-field (PCFF) is used, which can accurately simulate the structural, vibrational, and thermo-physical properties (e.g., phase transition temperature) of PE in both isolated and condensed phases.

Standard nonequilibrium MD (NEMD) is used to calculate the thermal conductivity of PE

structures by adding two Langevin thermostats are applied at the ends of the simulation domain to establish a temperature gradient across the sample. The thermal conductivity (κ) is calculated by Fourier's law, $\kappa = -J/(dT/dx)$, where dT/dx is the linear region temperature gradient of the steady state temperature profile and J is the heat flux obtained by tracking the thermostat energy flow (dQ/dt) over cross-sectional area. A 30 K temperature difference is chosen as no dependence of thermal conductivity on the temperature gradient is observed. All the simulations are carried out using the large-scale atomic/molecular massively parallel simulator (LAMMPS). A 0.25 fs time step is chosen due to the presence of fast vibrating hydrogen atoms. 40 PE chains with periodic boundary conditions in all three dimensions are simulated to yield a large enough cross-sectional area. Each PE chain consists of 200 monomers and is covalently bonded head-to-tail across the periodic boundary conditions to mimic infinitely long chain behavior.

To calculate the phonon dispersions, the structures below and above the phase transition temperature are quenched to 2 K using NVT ensemble. The atomic velocities of all the carbon atoms are recorded, and 2D fast Fourier transform is performed to convert time and position into frequency and wave vector respectively. To further illustrate the impact of phase transition on phonon scattering, we investigate the vibrational power spectra at three selected wave vectors. In comparison, peaks at 400 K (fig. S5), which correspond to the phonon eigen-frequencies, are significantly broadened. The scattering rates of the phonons is proportional to the broadening of these peaks, and the broadened peaks demonstrate the enhanced scattering in the disordered phases.

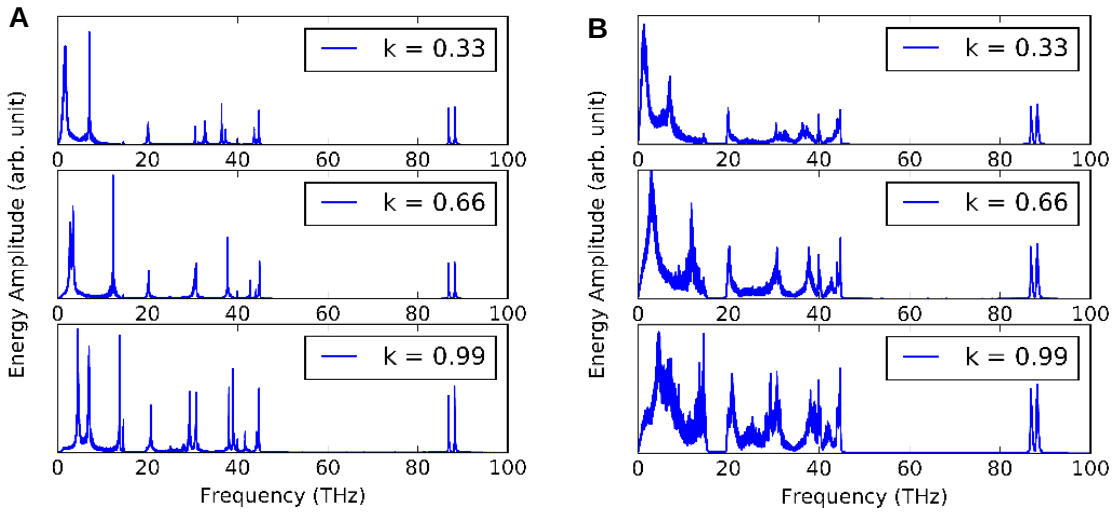

Fig. S5. The vibrational power spectra at three wave vectors before and after the phase transition of crystalline PE nanofibers. (**A**) 390 K and (**B**) 400 K. Narrow peaks in A indicate that phonons in the ordered structures have less scattering.

Figure S6 shows that the thermal conductivity of PE has a sharp drop around 400 K due to orthorhombic / hexagonal phase transition. This phenomenon is supported by experiments and MD studies as discussed in the main text. Within a 10 K temperature windows (390 K - 400 K), our MD simulations show that the phase transition induces the thermal conductivity change by a factor of 5.44 (5.14 W/mK at 400 K, 28.00 W/mK at 390 K).

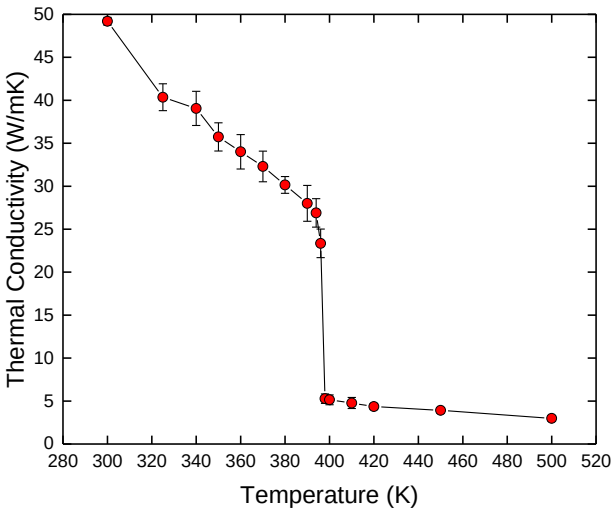

Fig. S6. Thermal conductivity of PE from 300 to 500 K.

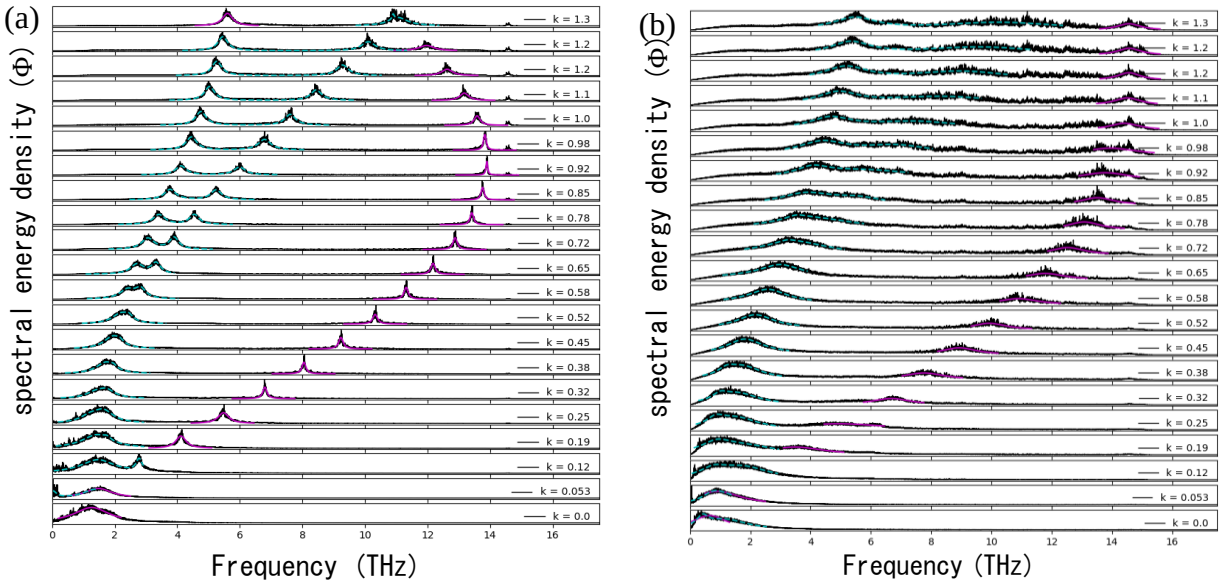

Fig. S7. Spectral energy density of PE at different k-points. (**a**) orthorhombic and (**b**) hexagonal phases.

The Boltzmann transport equation under the relaxation-time approximation with the Fourier law describes the thermal conductivity as a summation of phonon group velocity, phonon lifetime, and volumetric heat capacity over all photon modes. To further investigate these effects, 2D

Fourier transform is performed on the atomic velocities along the PE chain to yield phonon modal energy density as a function of wave vector and frequency. 21 k-points are selected, and the vibrational power spectra of acoustic phonons (< 20 THz) are plotted in fig. S7.

For each phonon mode, the range of frequencies spread of a peak is related to the anharmonicity of the interatomic potential and the corresponding rate of multi-phonon scattering processes. The shape of this frequency spread for each mode is the Lorentzian function

$$\Phi = \frac{\mathrm{I}}{1 + [(\omega - \omega_c)/\gamma]^2} \tag{S1}$$

where I is the peak magnitude, ω_c is the peak center location, and γ is the half-width of the peak. According to the above equation, the peak location and width of the spectral energy density are obtained from fig. S7. The orthorhombic and hexagonal phases show similar dispersion curves (figs. S8a and S8b), and thus the group velocities (slope of dispersion) are on the same order of magnitude (figs. S8c and S8d). On the other hand, the peak widths (shown as error bars in fig. S8b) of the hexagonal phases are significantly larger than those of the orthorhombic phase (shown as error bars in fig. S8a), indicating stronger phonon scattering and shorter lifetime in the hexagonal phases.

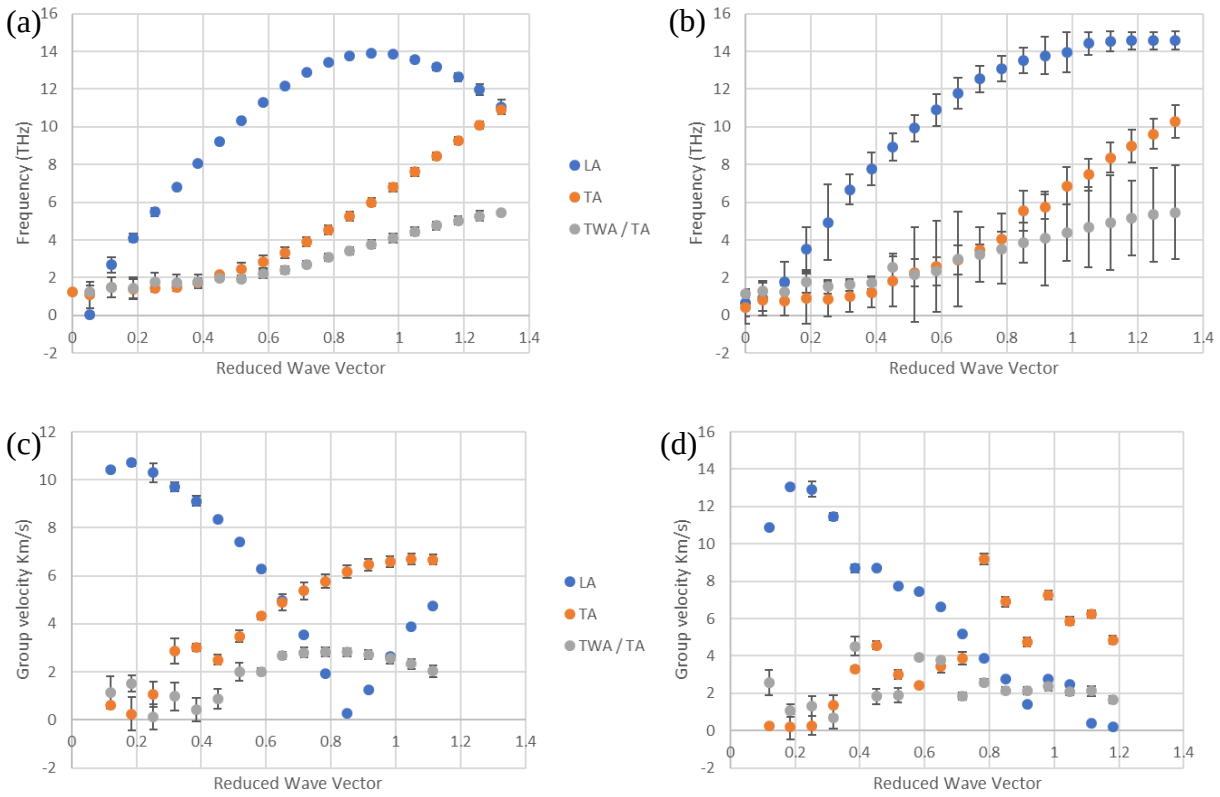

Fig. S8. Phonon dispersion and group velocity of PE. Phonon dispersion and peak width (as error bars) of PE in (**a**) the orthorhombic and (**b**) the hexagonal phases. Phonon group velocity of PE in (**d**) the orthorhombic and (d) the hexagonal phases.

The quantitative results are listed in Table S3. From the orthorhombic phase to hexagonal phase, the volumetric heat capacity and phonon group velocity change by only 5%, but phonon lifetime dramatically drops from 3.3 ps to 0.72 ps. Thus, the dominant mechanism for the giant thermal conductivity switching ratio (5.44) is the long phonon lifetime in the orthorhombic phase (4.58 times). Among different phonon modes, for example, longitudinal, traverse and torsional acoustic modes (LA, TA, TWA), the LA mode is found to be the main thermal energy carrier (72.46% of all acoustic modes) due to the large group velocity (5.97 over 4.18, 1.87) and phonon lifetime

(5.47 over 2.03, 2.10). Among all acoustic phonon modes, LA phonon mode is found to change by a factor of 8.22, dominating the thermal conductivity switching between the orthorhombic and the hexagonal phases.

Table S3. Thermal conductivity, volumetric heat capacity, phonon group velocity, and phonon life time.

	Orthorhombic Phase (390 K)	Hexagonal Phase (400 K)	Ratio (O/H)
Thermal conductivity (W/mK)	28.00	5.14	5.45
Volumetric heat capacity* (J $cm^{-3}K^{-1}$)	1.74	1.67	1.04
Phonon group velocity (Km/s)	3.47	3.67	0.95
Phonon lifetime (ps)	3.3	0.72	4.58
LA, TA, TWA / TA Phonon group velocity (Km/s)	5.97, 4.18, 1.87	5.98, 4.22, 2.25	1.00, 0.99, 0.75
LA, TA, TWA / TA Phonon lifetime (ps)	5.47, 2.03, 2.10	0.67, 0.68, 0.65	8.22, 3.05, 3.16

* represents from K. Loufakis, B. Wunderlcih, Polymer 26, 12 (1985).

It is worth noting that the phase transition temperature measured in our experiments (~435 K) is higher than the simulation data (~400 K). This is mainly due to the chain confinement effect in the nanofiber as the molecules are pined onto the measurement device, which greatly hinders the mobility of the chains. In addition, the stress on the specimen can shift the phase transition temperature. To investigate the thermal stability of PE fibers under stretching stress, difference pressures along the fiber directions are applied during the NPT simulations. Volume is recorded as the temperature increase. Figure S9 shows that the sharper volume jumps appear at higher temperature when fibers are stretched, indicating that pinning the ends of fibers (stretching) leads to better thermal stability and higher phase transition temperature.

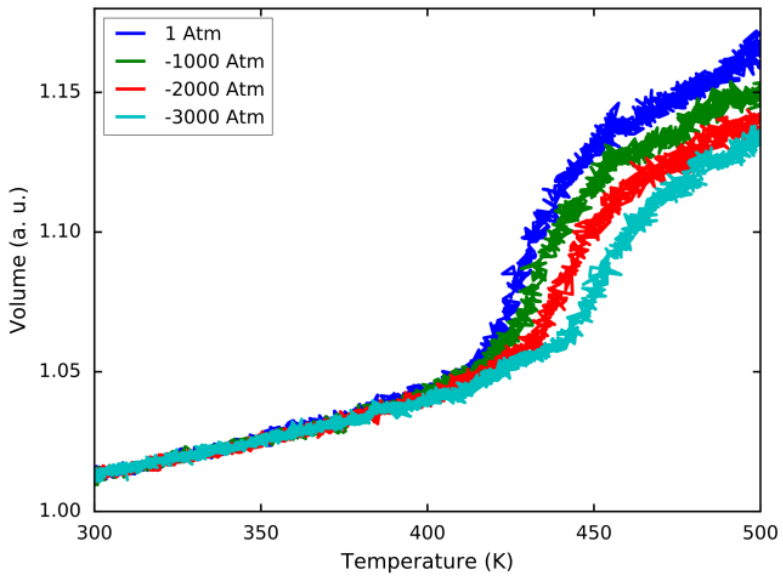

Fig. S9. Volume as a function of temperature when fibers are under stretching stress. As the ends of the fibers are pinned, stretching force (negative pressure) increases fiber thermal stability and the phase transition temperature.

7. Thermal contact resistance between the measurement islands and the nanofiber

To reduce the impact of thermal contact resistance between the measurement islands and the nanofiber, we employ the capillary-assisted adhesion by placing an isopropanol droplet on top of the microthermal device when placing the nanofiber. The calculation of the thermal contact resistance is based on the analysis in Ref. (*23*) using a line contact model. The thermal contact resistance of a typical PE nanofiber of 100 nm diameter is estimated to be $R_c \approx 5.5 \times 10^6$ KW^{-1} to 6.2×10^6 KW^{-1} before phase transition (fig. S10). This is consistent with the measured value in Ref. (*21*). Similarly, the thermal contact resistance after phase transition is predicted to be $R_c \approx 11.1 \times 10^6$ KW^{-1} to 19.2×10^6 KW^{-1}. From our thermal measurements in fig. 2B,

the thermal conductance of a ~100 nm diameter nanofiber is on the order of 10 nW/K and 1 nW/K before and after phase transition, respectively, which corresponds to the thermal resistances of 10^8 KW^{-1} and 10^9 KW^{-1}. In comparison, the measured overall thermal resistances before and after phase transition are generally 1-2 orders of magnitude larger than the thermal contact resistances. As a consequence, the change of the thermal resistance of the suspended fiber dominates the performance of the nanofiber thermal switches and diodes.

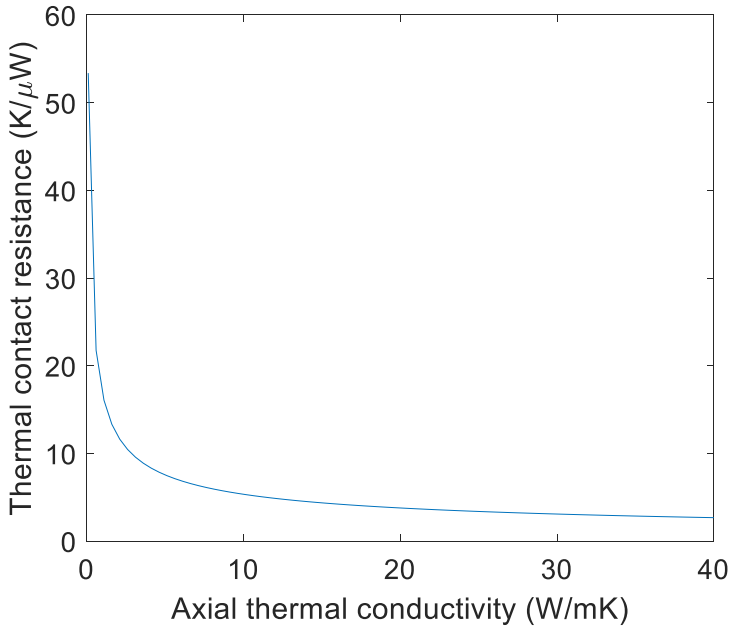

Fig. S10. Thermal contact resistance between the PE nanofiber and one suspended island as a function of the axial thermal conductivity of the PE nanofiber. The thermal contact resistance decreases with the increase of the axial thermal conductivity of the PE nanofiber.

8. Uniformity of the dimensions of suspended PE nanofibers

We measure the height of a suspended PE nanofiber between two suspended thermal measurement islands by Atomic Force Microscopy (AFM). The sample is measured by

non-contact mode. The typical radius of the tip (HQ: NSC15) is ~ 8 nm and the force constant of the cantilever is ~ 40 N/m. As seen in fig. S11, the height of the suspended PE nanofiber is 116.54 ± 0.98 nm, meaning that the height of the suspended PE nanofiber is pretty uniform along the whole length.

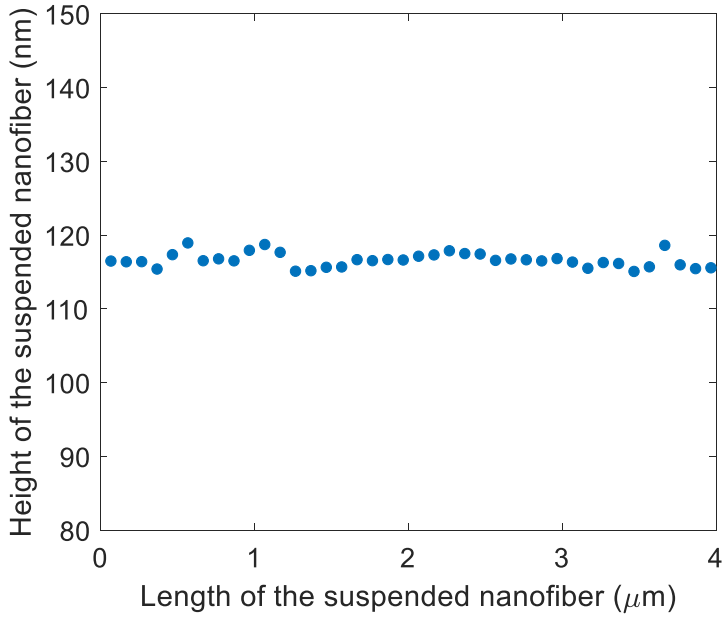

Fig. S11. The height map of a suspended nanofiber measured using atomic force microscopy. The height of the suspended nanofiber is very uniform along the length.

9. Uncertainty Analysis

The measurement of the thermal conductance of PE nanofibers at different temperatures is on the basis of the standard four-point I-V measurement developed by Ref. (*23*) and the Wheatstone bridge measurement developed by Ref. (*25*).

The reason is that the sensitivity of the Wheatstone bridge measurement is much higher (~20 times) than that of standard four-point measurement. In order to obtain a clear relation between

heat flux and temperature bias, we measure the Q-ΔT relation through the Wheatstone bridge measurement.

The calculation of uncertainty of thermal conductance of PE nanofibers is based on the analysis by Ref. (*23*), the thermal conductance *G* can be expressed as

$$G = \frac{Q}{(\Delta T_h - \Delta T_s)}\left(\frac{\Delta T_s}{\Delta T_h + \Delta T_s}\right) \tag{S2}$$

Where Q is the heat transferred to the heating island, T_s is the temperature of sensing island and T_h is the temperature of the heating island. Then the uncertainty of the thermal conductance is obtained

$$\left(\frac{\delta G}{G}\right)^2 = \left(\frac{\delta Q}{Q}\right)^2 + \left(\frac{\delta \Delta T_s}{\Delta T_s}\right)^2 + \left(\frac{\delta(\Delta T_h - \Delta T_s)}{(\Delta T_h - \Delta T_s)}\right)^2 + \left(\frac{\delta(\Delta T_h + \Delta T_s)}{(\Delta T_h + \Delta T_s)}\right)^2 \tag{S3}$$

At 400 K, the uncertainty of heat transferred to the heating island is less than 0.07%. The uncertainty of ΔT_s is ~ 0.64%, $\Delta T_h - \Delta T_s$ is ~ 3.01% and $\Delta T_h + \Delta T_s$ is ~ 0.98%. Therefore, the uncertainty of thermal conductance in our case is

$$\frac{\delta G}{G} = \sqrt{\left(\frac{\delta Q}{Q}\right)^2 + \left(\frac{\delta \Delta T_s}{\Delta T_s}\right)^2 + \left(\frac{\delta(\Delta T_h - \Delta T_s)}{(\Delta T_h - \Delta T_s)}\right)^2 + \left(\frac{\delta(\Delta T_h + \Delta T_s)}{(\Delta T_h + \Delta T_s)}\right)^2}$$

$$= \sqrt{(0.07 \times 10^{-2})^2 + (0.64 \times 10^{-2})^2 + (3.01 \times 10^{-2})^2 + (0.98 \times 10^{-2})^2}$$

$$= 3.23\%$$

The noise-equivalent temperature (NET) in four probe measurement is

$$\mathrm{NET} = \frac{\mathrm{NER}_s/\mathrm{R}_s}{\mathrm{TCR}} \tag{S4}$$

In our case, the $\mathrm{NER_s/R_s}$ is found to be ~ 7.5×10^{-5}. The temperature coefficient of resistance (TCR) of the PRT is ~ 0.002/K. Therefore, the NET is ~ 37.5 mK at 400 K.

Then the noise-equivalent thermal conductance (NEG_s) can be obtained as follows

$$\mathrm{NEG}_s = G_b \frac{\mathrm{NET}}{\Delta T_h - \Delta T_s} \approx 1.01\mathrm{nW/K} \tag{S5}$$

Where G_b is the conductance of the suspending beams (~135 nW/K), and $\Delta T_h - \Delta T_s$ is the temperature difference between the heating and sensing islands (~5 K).

In our experiment for the thermal performance of thermal switches and diodes, we use the Wheatstone bridge measurement to obtain a more accurate data. Provided that the input noise of the SR830 amplifier is 5 nV/$\sqrt{\mathrm{Hz}}$ and the equivalent noise bandwidth (denoted as Δf) is around 0.3 Hz, the noise at the amplifier input can be

$$N_{amp} = \left(5\ nV/\sqrt{\mathrm{Hz}}\right) \cdot \sqrt{\Delta f} = 2.74\ \mathrm{nV} \tag{S6}$$

And the Johnson noise of each resistor is obtained by

$$N_{J,i} = \sqrt{4k_B T_i R_i \Delta f} \tag{S7}$$

Where T_i is the temperature of the resistor R_i. And in our experiment $T_s = T_1 = 400K$, $T_3 = T_4 = 300K$, $R_1 = 1.826\ \text{k}\Omega$, $R_s = 4.499\ \text{k}\Omega$, $R_3 = 3.05\ \text{k}\Omega$, $R_4 = 3.02\ \text{k}\Omega$. Therefore, the total voltage noise at lock-in input is the summation of all the above noise sources

$$\Delta V_g = \sqrt{\sum_i N_i^2} \approx 16.5\ \text{nV} \tag{S8}$$

When the resistance value is much larger than the change in resistance, the change of R_s can be calculated as

$$\Delta R_s = \left(\frac{\Delta V_g}{V_s}\right)\frac{(R_s + R_2)^2}{R_2} \approx 15.5\ \text{m}\Omega \tag{S9}$$

Based on the measured TCR of the platinum coil (0.002/K), the noise equivalent temperature (NET) can be obtained as

$$\text{NET} = \frac{\Delta R_s}{R_s}\frac{1}{\text{TCR}} \approx 1.92\ \text{mK} \tag{S10}$$

Then the noise equivalent conductance (NEG_s) can be calculated as follows

$$\text{NEG}_s = G_b \frac{\text{NET}}{\Delta T_h - \Delta T_s} \approx 52.9\ \text{pW/K} \tag{S11}$$

Here, G_b is the conductance of the suspending beams (~135 nW/K), and $\Delta T_h - \Delta T_s$ is the temperature difference between the heating and sensing islands (~5K).

10. Micro-Raman measurement of the PE microfiber

We also performed the micro-Raman measurements on PE microfibers, as shown in fig. S12. The PE microfiber has a lower degree of crystallinity with a higher peak around 1440 cm^{-1}. However, the phase transition of the PE microfiber was not captured in our experiment because its phase transition temperature is very close to the melting point of the microfiber, and the microfiber broke at 430 K during the measurement.

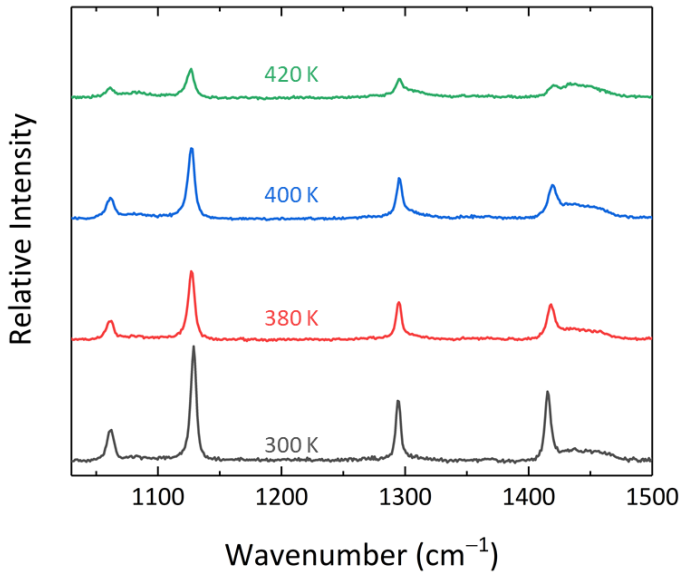

Fig. S12. Raman spectra in the temperature range from 300 to 420 K. The microfiber was damaged at 430K.